Atomistic study of stability of xenon nanoclusters in uranium oxide

A. Chartier,[1,*] L. Van Brutzel,[1] and M. Freyss[2]
[1]*DEN, Service de Chimie Physique, CEA, F-91191 Gif-sur-Yvette, France*
[2]*DEN, Service d'Études et de Simulation du Comportement des Combustibles, CEA, F-13108 Saint-Paul lez Durance, France*
(Received 24 November 2009; revised manuscript received 8 February 2010; published 12 May 2010)

Density-functional theory calculations of the xenon incorporation energies in point defects in urania have been done in order to fit empirical potentials. With this set of parameters, we have considered the incorporation of xenon in small and extended defects such as planar interstitials, grain boundaries, faceted, and spherical voids. The results show that xenon atoms are more likely to aggregate than to be homogeneously distributed in the urania grains. Σ5 grain boundary and spherical shape voids are the most favorable defects of xenon atom incorporation. The presence of xenon atoms in nanovoids affects their shape. The energy gain to aggregate xenon atoms into clusters saturates for cluster sizes of about 15–20 Schottky defects. This demonstrates that medium size defects are just as favorable as big size defects for xenon incorporation.

DOI: 10.1103/PhysRevB.81.174111 PACS number(s): 61.80.−x, 61.72.Nn, 61.72.Qq

I. INTRODUCTION

Xenon is a major fission product in the standard nuclear fuel UO_2. It is, for a large part, responsible for the structural (i.e., swelling) and physical (i.e., thermal conductivity) modifications of the fuel during both reactor operation and long-term storage. Therefore, a good prediction of the release of this fission gas from the nuclear-fuel matrix UO_2 is essential. For low and medium burnups, there is a widely accepted picture of fission-gas release behavior based on the early Booth sphere model[1] and on its further improvement developed by White and Tucker.[2] A simplified scheme can be summarized as follow: fission gas is uniformly generated within the fuel grain. Because it is nearly insoluble in fuel matrix, single atoms diffuse to form intragranular bubbles which may be created and destroyed by fission spikes. The gas atoms can further diffuse into the grains reaching the grain boundaries to form larger intergranular bubbles which percolate and escape into the rod voids. However, for higher burnups this picture fails and the details of xenon intragranular and intergranular behavior are still unclear. Those behaviors estimated from experimental observations and by comparison with metals are the key inputs used in macroscopic models implemented, for example, in MFPR code (Refs. 3–5), MARGARET code (Ref. 6), or in several other continuous models (see, e.g., Ref. 7). The meaning of each term used in those models is still under debate. The reason is mainly due to the difficulties associated with setting up experiments at the atomic scale on irradiated or implanted materials (see, for example, Refs. 8–14) in order to obtain microscopic details.

The use of atomistic simulations can be an alternative in obtaining a reliable insight into the basic mechanisms. Twenty year ago, Catlow and co-workers[15–18] studied extensively the trapping mechanism of xenon atoms by point defects in urania. These studies showed that isolated point defects are thermodynamically driven to aggregate and that xenon atoms are more likely to precipitate into Schottky defects rather than into isolated vacancies. More recently, this kind of simulation has regained consideration. For instance, the homogeneous resolution mechanisms of intragranular xenon fission gas bubbles have been revised using classical molecular-dynamics (MD) simulations.[19,20] Schwen *et al.*[19] report a resolution parameter that is 50 times lower than past estimates. Other studies using molecular-dynamics simulation show the stability of xenon in planar configurations in UO_2.[21] Nevertheless, questions such as what is the basic mechanism of xenon bubble formation and where the bubbles initiate still remain open.

The present paper aims at bringing insights into these two latter questions using static calculations with empirical potentials. In the following, we present interatomic potentials for Xe-U and Xe-O interactions which have been fitted upon first-principles calculations of xenon incorporation energies into basic point defects. We then describe the empirical potential calculations of the incorporation energies of xenon in extended defects such as faceted and spherical voids, grain boundary, and planar interstitials. The results are finally discussed comparing the incorporation energies of xenon in the various defects considered.

II. COMPUTATIONAL PROCEDURE

First we have carried out first-principles density-functional-theory (DFT) calculations with the generalized gradient approximation (GGA) approximation[22] for single point defects and xenon incorporation in UO_2. A $2\times2\times2$ supercell containing 96 atoms have been used for this study. The electronic structure and total energy of the system were calculated using the projector augmented waves (PAW) method[23] as implemented in the code VASP.[24] A 450 eV cutoff energy was chosen to truncate the plane-wave-basis set of the valence electrons and a $4\times4\times4$ Monkhorst-Pack *k*-point grid to sample the irreducible Brillouin zone of the supercell. Xenon atoms were incorporated at various sites of the UO_2 fluorite lattice: the uranium and oxygen substitution sites and the octahedral interstitial site. For each of these configurations, the atomic positions and the volume of the supercell were relaxed.

The DFT-GGA results reported herein can be considered more reliable than those published previously by Freyss *et al.*[25] Because PAW method is more accurate than the Troullier-Martins pseudopotential method[26] and larger super-

cells were used here. However, the DFT-GGA fails to describe urania as an insulator and a way to reproduce its insulating behavior and better treat the strong correlations of the $5f$ electrons would be to use the DFT+U method[27] or hybrid functionals.[28] Unfortunately, those latter methods induce the existence of metastable states according to the occupation of the $5f$ orbitals, which makes the convergence to the electronic ground state difficult, even impossible in some cases. The discrepancies found in the already published DFT+U studies of point defects[29–33] or xenon atoms incorporation in urania[34,35] reflect this issue and are a hint that the convergence was not monitored carefully enough. To avoid metastable states and systematically reach the ground state of uranium dioxide with DFT+U, Dorado *et al.*[36] showed that the monitoring of occupation matrices is crucial, as well as allowing the $5f$ electrons to break the cubic symmetry. This procedure was still too computationally demanding to be applied to xenon atom incorporation in urania for the fitting of the empirical potentials used herein. But by comparing the DFT-GGA results on xenon atoms in urania obtained here with those subsequently published using DFT+U,[34,35] we will see that they are reliable enough for the generation of empirical potentials.

The incorporation energy of xenon in the interstitial site, noted later Xe(I), is defined as follows:

$$\mathrm{Xe_g} + n\mathrm{UO_2} \rightarrow \mathrm{U_nO_{2n}Xe(I)}$$

with

$$E_{\mathrm{inc}}[\mathrm{Xe(I)}] = E[\mathrm{U_nO_{2n}Xe(I)}] - nE(\mathrm{UO_2}) - E(\mathrm{Xe_g}), \quad (1)$$

where $nE(\mathrm{UO_2})$ is the energy of the defect-free supercell, $E[\mathrm{U_nO_{2n}Xe(I)}]$ is the total energy of the supercell containing one xenon atom trapped at one of the octahedral interstitial sites, $E(\mathrm{Xe_g})$ is the energy of the isolated xenon atom in a gaseous reference state, and n the number of $\mathrm{UO_2}$ patterns in the supercell. Note that the energy $E(\mathrm{Xe_g})$ is zero for the empirical potential. Similar equations are written for the incorporation energies of xenon in vacancies. For example, the incorporation energy of xenon in a uranium vacancy [quoted Xe(V_{U})] reads as

$$\mathrm{Xe_g} + \mathrm{U_{n-1}O_{2n}} \rightarrow \mathrm{U_{n-1}Xe}(V_{\mathrm{U}})\mathrm{O_{2n}}$$

with

$$E_{\mathrm{inc}}[\mathrm{Xe}(V_{\mathrm{U}})] = E[\mathrm{U_{n-1}Xe}(V_{\mathrm{U}})\mathrm{O_{2n}}] - E(\mathrm{U_{n-1}O_{2n}}) - E(\mathrm{Xe_g}) \quad (2)$$

where $E(\mathrm{U_{n-1}O_{2n}})$ is the total energy of the system containing one uranium vacancy and where $E[\mathrm{U_{n-1}Xe}(V_{\mathrm{U}})\mathrm{O_{2n}}]$ is the total energy of the system containing the xenon atom into the uranium vacancy. The results of the DFT+U calculations are reported in Table I and they are compared to other recent DFT calculations. Despite significant differences between the DFT+U values, as discussed above, the results are consistent with each other and show the same trend. As already shown by Freyss *et al.*[25] or by Yun *et al.*[37] using the GGA approximation, xenon atoms are insoluble in the $\mathrm{UO_2}$ matrix and are more stable in the uranium vacancies than in the oxygen vacancies, and even more stable than in interstitial sites. Furthermore, the DFT-GGA calculations by Yun *et al.*[37] show that the lowest incorporation energy is found for xenon in a neutral trivacancy where the two oxygen vacancies and the uranium vacancy are first nearest neighbors, called Schottky defect and denoted S in the following.

TABLE I. Xenon incorporation energies (E_{inc}) in the $\mathrm{UO_2}$ matrix for simple point defects (octahedral interstitial sites I, vacancies V, and Schottky defects S) calculated using DFT calculations and empirical potentials.

	E_{inc} (eV)			
Defects	Xe(I)	Xe(V_{U})	Xe(V_{O})	Xe(S)
Empirical potential	11.92	5.40	9.34	4.21
Present DFT GGA	12.01	5.77	9.14	
DFT+U[a]	11.1	2.5	9.5	1.38
DFT+U[b]	8.07	5.18	9.01	2.90

[a]Reference 34.
[b]Reference 35.

We turn now to the calculations done with empirical potentials. The interactions for the description of pure $\mathrm{UO_2}$ are taken from the potentials developed by Morelon *et al.*[38] These potentials have been fitted to reproduce best the formation and the migration energies of single point defects from *ab initio* calculations[39] and from experiments.[40] It agrees also well with the crystal-structural properties as reported by Govers *et al.*[7,41]

The Xe-Xe interaction is described with the potential developed by Tang and Toennies.[42] This potential is based on an accurate description of the Van der Waals interactions calculated with high-level *ab initio* methods. To assess this potential for our specific case (pressurized xenon bubbles), we have investigated the effect of pressure on the xenon gas and on solid xenon. The results reported on Fig. 1 are compared with available experiments[43,44] and show that the Tang and Toennies potential can reasonably reproduce both behaviors up to 50 GPa.

Finally, we have chosen to use the Buckingham potentials for the Xe-U and the Xe-O interactions

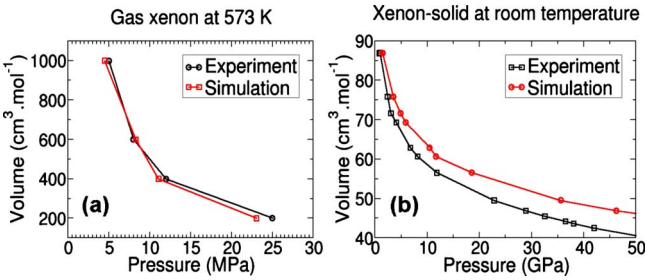

FIG. 1. (Color online) Comparison between experimental values and calculated values of the state equation of xenon in (a) gas and (b) solid state. The experimental data were taken from Baettie *et al.* (Ref. 43) for the gas and Zisman *et al.* (Ref. 44) for the solid.

TABLE II. Parameters of the Buckingham potentials for Xe-U and Xe-O interactions.

A (eV)		ρ (Å)	
Xe-O	Xe-U	Xe-O	Xe-U
94.489	478875.11	0.58	0.179

$$V_{\text{Xe-U/Xe-O}}(r_{ij}) = A_{\text{Xe-U/Xe-O}} \exp\left(-\frac{r_{ij}}{\rho_{\text{Xe-U/Xe-O}}}\right). \quad (3)$$

The A and ρ parameters were fitted to reproduce the xenon incorporation energies obtained by the DFT-GGA calculations, using the same size cells. The results of the incorporation energies are reported in Table I and the resulting parameters in the Table II. All the following static calculations were carried out with the code GULP.[45] As can be seen on Table I, the fitted potentials reasonably reproduce the incorporation trend obtained by first-principles calculations, whether obtained with DFT or DFT+U. The DFT results by Yun *et al.*[37] were not reported in Table I because they used other expressions to calculate the incorporation energies of xenon thus avoiding a direct comparison. Note that the incorporation energy in Schottky defect obtained using the present potential is overestimated by 1.5–3.0 eV compared to the DFT+U calculations. This is not a real issue for the results presented below as the incorporation energy in Schottky defects remains the lowest.

To crosscheck the reliability of the potentials, the volume expansions of the 96-atom urania supercells containing a single xenon atom in point defects have been calculated and compared with DFT+U first-principles calculations[35] (see Table III). The empirical potentials give the same behaviors as the DFT and DFT+U first-principles calculations. Xenon atoms trapped in both an oxygen vacancy and in an octahedral interstitial site have the highest and similar volume expansion whereas xenon atoms trapped in uranium vacancy have the lowest.

III. POINT DEFECTS

In order to complete the analysis of the xenon stabilization in point defects, we have calculated the binding energies of some point defects in pure urania and the binding energies of point defects containing xenon atoms. With empirical potentials the charges on the atoms are fixed, therefore the system energy is minimal for neutral defects. Hence, only neutral defects have been studied herein. The results are reported in Table IV.

TABLE III. Comparison of the swelling ($\Delta V/V_0$) after relaxation of the urania 96-atom supercell with xenon atom in several point defects (octahedral interstitial sites I, vacancies V, and Schottky defects S), between empirical potential calculations and DFT calculations.

	Swelling (%)			
Defects	Xe(I)	Xe(V_U)	Xe(V_O)	Xe(S)
Empirical potential	2.2	1.0	2.2	1.1
Present DFT GGA	2.7	1.4	2.6	
DFT+U[a]	2.4	0.6	2.8	1.5

[a]Reference 35.

In general, we find that defects release energy when they aggregate, independently of whether or not they contain xenon atoms. For instance, the aggregation of two isolated oxygen interstitials and one uranium interstitial to an anti-Schottky (noted AS) where the three interstitials are first nearest neighbor is found to release an energy of 3.2 eV. The same behavior is found for the neutral trivacancy (S for Schottky) which releases an energy of 3.1 eV. This value is in good agreement with the value (3.8 eV) found by Dorado *et al.*[33] using DFT+U calculations but a bit lower than the one (5.1 eV) found by Nerikar *et al.*[34] The aggregation of two isolated AS defects or two S defects release as well some energy: 2.2 and 2.8 eV, respectively. In both cases, we have considered several configurations of the oxygen vacancies, respectively, the oxygen interstitials around the uranium vacancy, respectively, the uranium interstitial. However, in both cases the configuration changes produce small contributions to the binding energies (approximately 0.1–0.2 eV) and thus the Schottky (respectively, anti-Schottky) configurations will not be considered in the following. For the aggregation of two S defects, the arrangement of oxygen vacancies show that the lower energy is obtained as soon as the compacity of the vacancies (both uranium and oxygen vacancies) is the highest. The most stable configuration is the one with the uranium vacancies as first neighbors and with two of the four oxygen vacancies in between. These results are consistent with older works carried out by Catlow *et al.*[15,18] in which different empirical potentials interactions have been used. The reverse is true for the aggregation of two AS: the energy is lower as soon as the compacity of the oxygen interstitials is the lowest around the two first neighbors uranium interstitials.

TABLE IV. Upper part: binding energies of neutral point defects. AS stands for anti-Schottky defects where all the interstitials are first nearest neighbor. S stands for Schottky defects where all the vacancies are first nearest neighbor. Lower part: binding energies of point defects containing xenon atoms.

Pure UO_2	Defects	$2I_O+I_U-AS$	$2AS^{\infty}-2AS^{1st\ neig}$	$2V_O+V_U-S$	$2S^{\infty}-2S^{1st\ neig}$
	$E_{binding}$ (eV)	−3.2	−2.2	−3.1	−2.8
UO_2+Xe	Defects	$2Xe(I)^{\infty}-2Xe(I)^{1st\ neig}$		$2Xe(S)^{\infty}-Xe(S)^{1st\ neig}$	
	$E_{binding}$ (eV)	−1.1		−2.9	

These results mean that isolated point defects tend to aggregate in urania. Therefore, point defects will form nanovoids (aggregation of Schottky defects) and dislocations (aggregation of anti-Schottky defects) instead of being homogeneously distributed in the grains.

IV. PLANAR DEFECTS

A. Virgin surfaces and interfaces

We first consider the formation energies of virgin (i.e., xenon free) surfaces/interfaces calculated using the present empirical potentials. These formation energies will be used to build the nanovoids shape using the Wulff construction[46] (see Sec. V). Four surfaces—namely, the {110}, {111}, {100}, and {310} surfaces—have been investigated. The {110}, {111}, and {100} surfaces are type I, II, and III in the Tasker's classification.[47] All the surfaces were relaxed with static minimization of the energy. In the case of the {100} surfaces, this relaxation leads with an equal probability to the same three different surface-structure configurations A, B, and C described in Ref. 48. Therefore, the reported formation energies for the {100} surface (see below) is the average value of the three configurations.

We have calculated also the formation energy of the virgin symmetrical tilt grain boundary (GB) Σ5 with static energy minimization at constant volume. The formation energy of the Σ5 GB will be used as a reference for the incorporation of xenon in the following section. This specific GB was chosen in light of the previous results (obtained using the same empirical potentials see Ref. 49) which demonstrated that it is the most stable GB in UO_2. The procedure employed (for more details see Ref. 49) to generate this GB started by its relaxation using MD simulations in the NPT ensemble at 300K. The analysis of the structure evidenced[49] a sliding of both crystals relative to one another along the GB plane during the relaxation. This sliding was shown[49] to be responsible for the creation of Schottky defects at the GB interface. Despite the simplicity of such a procedure (compared to a more sophisticated one, see Ref. 50), this relaxation allows to get a structure hopefully close to the optimal GB. In fact, the structure of the Σ5 GB obtained by MD (Ref. 49) mimics in very details the structure observed in the structurally related yttria-stabilized zirconia.[51]

The surfaces (and GB) formation energies were calculated as follows:

$$\gamma_{\text{plane}} = \frac{E_{\text{plane}} - E_{\text{UO}_2}}{2A}, \tag{4}$$

where E_{UO_2} is the energy of the perfect crystal, E_{plane} is the energy of the crystal containing two defective planes (either the surfaces or the GB), and A is the surface area of the plane. Because the periodic boundary conditions are used, two surface areas need to be counted. The calculations were done by static minimizations of the energy at constant volume.

In order to investigate the cell-size effects, several calculations of the surface-formation energies and the Σ5 GB formation energies were done with different distances between both surfaces/GB. The results for the Σ5 GB are displayed in Fig. 2. The surface energy decreases with the increasing distance between the planes. However, saturation seems to appear at a distance of about 5 nm between planes. These results show the importance of computing in large cells to avoid size effects. Generally, the interface (surface and GB) energies vary as the inverse of the distance, d^{-1}, between the planes.[52] Streitz[53] added a quadratic dependence on the inverse of the distance, as d^{-2}. Thus the formation energy of planar defects may be written as

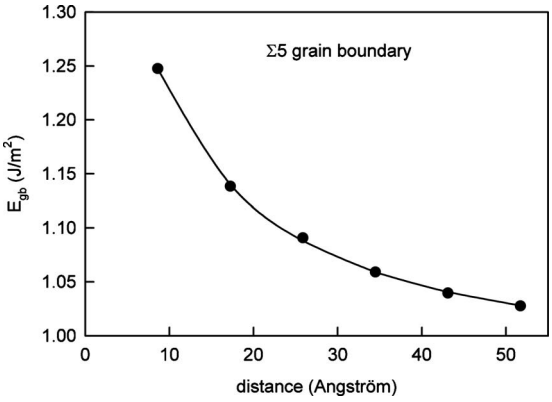

FIG. 2. Formation energy γ of the Σ5 grain boundary (in J/m^2) as a function of the distance between both interfaces. The continuous line is the result of the fit using Eq. (5).

$$\gamma(d) = \gamma^{\infty}_{\text{plane}} + \frac{f}{d} + \frac{f'}{d^2}, \tag{5}$$

where γ^{∞}, f, and f' are three parameters. Those parameters depend upon the elastic constants of bulk UO_2. The f and f' parameters are related to the surface (interface) shear stresses and to the volume stresses induced by the two interfaces in the supercell, respectively. This equation fits perfectly the data calculated (line fit in Fig. 2).

The formation energies γ^{∞} of the surfaces and the Σ5 grain boundary are reported in Table V. As previously shown by Abramowski *et al.*,[48] the lowest surface-formation energy is found for the {111} surface. The other surface-formation energies are in the range of those found using other potentials[48] (cf. Table V). The energy ratio between the {111} and the {100} surfaces is 1.16 in the present calculations,

TABLE V. Formation energies γ^{∞}(J/m^2) of four surfaces and of the Σ5 grain boundary of urania.

Surface (J/m^2)	This work	Ref. 48
{111}	1.71	0.89–1.48
{100}	1.99	1.43–3.84
{110}	2.38	1.28–2.25
{310}	3.78	1.76–3.30
GB (J/m^2)	**This work**	
Σ5	0.96	

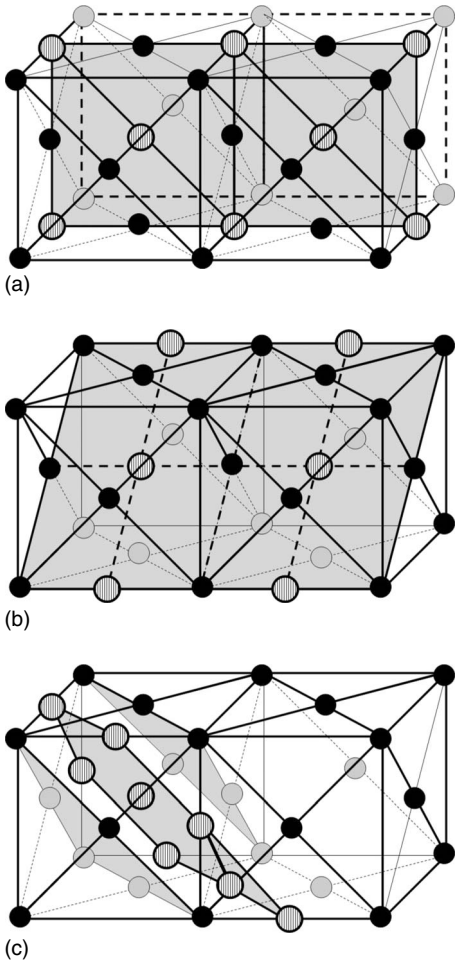

FIG. 3. Schematic view of the xenon atom insertion (open hatched spheres) into (a) the {100} plane, (b) the {110} plane, and (c) the {111} plane of urania. For clarity only the fcc uranium sublattice (filled spheres) is represented.

close to the value of 1.42 found experimentally.[54] It should nevertheless be kept in mind that the "trench configuration" of the {100} surface, not calculated here, may contribute drastically to the energy ratio between the surfaces as shown by Tan *et al.*[55] Finally, the formation energy of the Σ5 GB is twice as low as the formation energy of the {111} surface. This is consistent with the fact that in pure UO_2 the formation of Σ5 GB is more likely than any free surfaces.

B. Xe incorporation in planes

We now turn to the incorporation of xenon in the three {100}, {110}, and {111} planes and in the Σ5 grain boundary. The xenon atoms were introduced in interstitials sites along those planes, as shown in Figs. 3(a)–3(c). The number of xenon atoms introduced was chosen to keep approximately the same densities of xenon in each plane (cf. Table VI). The definition of the incorporation energy of *p*-Xe atoms into *p* interstitial sites along planes is a generalization of Eq. (1)

TABLE VI. Xenon incorporation energies in three different planes and in the Σ5 grain boundary. The values are from the fits done using Eq. (5).

Surfaces	Density (Xe/Å^2)	E_{inc}^{∞}(Xe) (eV)
{100}	0.066	12.4
{110}	0.047	5.2
{111}	0.067	2.5
Σ5	0.085	0.07

$$pXe_g + nUO_2 \rightarrow U_nO_{2n}pXe(I)$$

with

$$E_{inc}[Xe(I)^p] = \{E[U_nO_{2n}pXe(I)] - nE(UO_2) - pE(Xe_g)\}/p. \quad (6)$$

The minimization of the energies was carried out at constant volume. The incorporation energies per xenon atom are reported as a function of the distance between the planes of incorporation on Fig. 4. As already stated in the previous section for the surfaces and Σ5 GB, the incorporation energies decrease as a function of the distance between the planes. This is due to the fact that the interaction energies between the planar defects decrease as a function of their distance. The incorporation energies of xenon for noninteracting planar interfaces (noted with the symbol ∞) were calculated using the Eq. (5) and are reported in Table VI.

Except for the {100} plane the xenon incorporation energies in planes are smaller than the xenon incorporation energy in an isolated interstitial site $\{E_{inc}[Xe(I)]=11.92$ eV$\}$, which is represented by the horizontal dashed line in Fig. 4. This result is consistent with the gain in energy of 1.1 eV

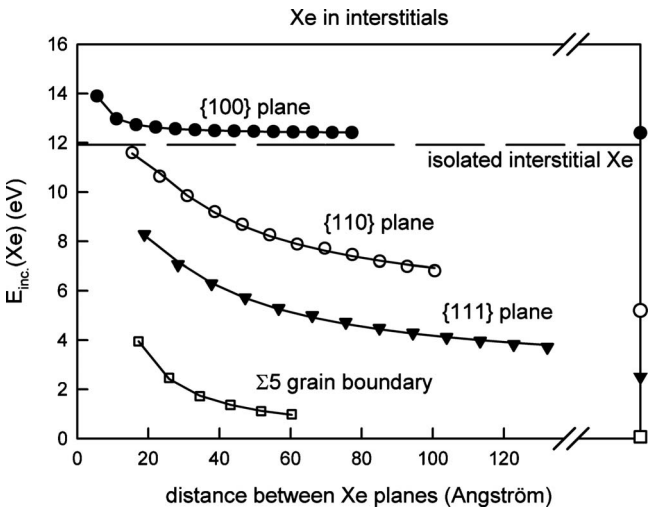

FIG. 4. Xenon incorporation energies in {100}, {110}, and {111} planes and in Σ5 grain boundary as a function of the distance between the planes. The lines are fits using Eq. (5). The horizontal dashed line is the incorporation energy of an isolated xenon atom in an interstitial site. The symbols on the right *y* axis are the incorporation energies E_{inc}^{∞}(Xe) quoted from Table VI.

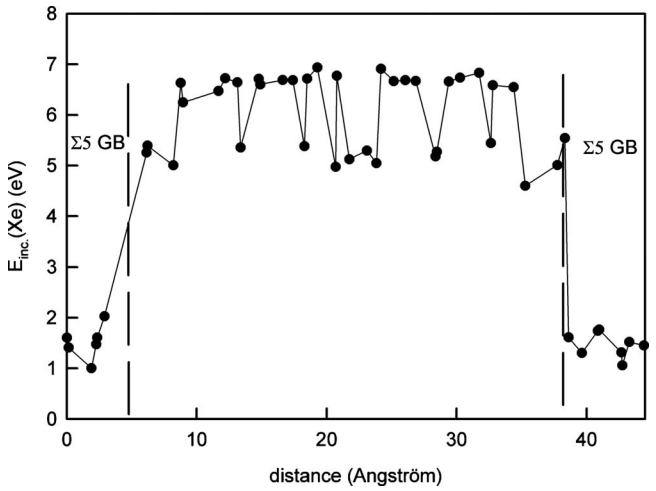

FIG. 5. Xenon incorporation energies in and between two Σ5 parallel grain boundaries distanced by 44.4 Å as a function of the distance from one of the Σ5 interface.

obtained for the aggregation of two isolated xenon in interstitial sites (cf. Table IV). In fact, this means that xenon atoms will preferentially stabilize in extended planes instead of staying homogeneously distributed in the urania matrix.

The lowest xenon incorporation energy is found for the Σ5 grain boundary. Consequently, xenon atoms tend to stabilize in the Σ5 grain boundary rather than in the urania grains or other interfaces. We have calculated the incorporation energy of xenon as a function of its distance from the Σ5 grain boundary (see Fig. 5). In this figure, we see that the gain in energy starts to be significant for a distance lower than approximately 1 nm from the GB interface. As previously presented by Van Brutzel *et al.*[49,56] the structure of the Σ5 GB is composed of Schottky-type defects. Moreover, the xenon incorporation energy in Schottky defects is the lowest (cf. Table I). Hence, it is not surprising to find that a Σ5 grain boundary is the most favorable planar defect for the incorporation of xenon atoms.

V. INCORPORATION OF XENON IN VOIDS

At thermal equilibrium, some vacancies are present in the lattice of urania. However, their concentration is low enough to consider each vacancy as isolated. Under irradiation, the picture is different. Each irradiation event participates to the creation/annealing of numerous defects and also to their enhanced diffusion. The aggregation (or destruction) of nanovoids, and then possibly, the precipitation (or resolution) of xenon atoms into (or from), thus these nanovoids may occur more easily. However, the shape of the nanovoids in which xenon precipitates is not yet fully known.

Before considering the incorporation of xenon in voids, we have investigated the formation energy of empty voids. As already mentioned in Sec. II, connecting two isolated oxygen vacancies to one uranium vacancy as first nearest neighbor releases an energy of 3.1 eV. Therefore, we have chosen this particular Schottky defect, noted S, as the elementary brick to construct voids.

A. Spherical and Wulff-shaped voids

We have built various shapes of voids (without xenon inside) in a 1500-atom supercell ($5\times5\times5$ conventional cell). The spherical voids have been built by removing S defects in a sphere of increasing radius without considering the compacity criterion for the oxygen vacancies arrangement. In general, oxygen vacancies rearrange during optimization. In principle, other starting configurations could be considered to build spherical voids but we have limited ourselves to this particular case as it is generic to the behavior of spherical voids. Voids made with specific nonspherical surfaces were investigated as well. We considered cubic three-dimensional (3D) voids made only with one of the {100}, {110}, or {111} surfaces and a case were the ratio between surfaces obeys the Wulff construction.[46] In the specific case of the {100} 3D voids, the oxygen ions reorganize themselves in order to avoid any dipole effect, as already seen for the surfaces. We will not go in deeper details as the {100} 3D voids are energetically less favorable than the others voids (see below). Finally, we investigated disk-shaped voids [two-dimensional (2D) voids] of increasing radius parallel to the {111} plane. All the calculations were done at constant volume.

For all these types of voids, we calculated the binding energy as a function of the number p of S defects. The binding energy (BE) of all the voids is expressed as follows:

$$p \times \mathrm{S} \rightarrow \mathrm{Void}_{\mathrm{p}}^{\mathrm{S}}$$

with

$$E_{\mathrm{binding}}(\mathrm{Void}_{\mathrm{p}}^{\mathrm{S}}) = [E(\mathrm{Void}_{\mathrm{p}}^{\mathrm{S}}) - pE(\mathrm{S})]/p, \qquad (7)$$

where $\mathrm{Void}_{\mathrm{p}}^{\mathrm{S}}$ is a void made of pS defects. The maximum size of the 3D voids is limited to 30 S defects (90 atoms, 6% of atoms removed). This number of S defects corresponds to a spherical nanovoid of 1.5 nm of diameter. It has also been chosen to avoid any self-interactions caused by the periodic boundary conditions. In general, the self-interaction is low. For instance, for a 9 S spherical void (as defined above) in supercells of 324 atoms (8% of atoms removed) up to 4116 atoms (0.6% of atoms removed) the self-interaction varies by less than 0.01 eV per S defect. We have limited also the size of 2D voids to 20 S defects in order to avoid planar self-interactions.

The BE as a function of the number p of S defects are reported on Fig. 6. The BE of (almost) all the voids are negative and decrease as a function of the number p of S defects. This confirms that S defects tend to aggregate in urania. The cubic voids made of {100} planes are the least stable, which is surprising considering that the formation energy of the {100} surface is not the highest (cf. Table V). Conversely, the BE of the cubic voids made of {110} planes are among the lowest while their surface formation energy is the highest (cf. Table V). The disk-shaped voids (2D voids) are also less stable than the other 3D voids. For all the other types of voids, the BEs are comparable to one another. We can see a relative increase in the BE for the spherical voids consisting of more than 20 S defects, compared to the cubic {110}-, {111}-, and Wulff-shaped voids, in agreement with

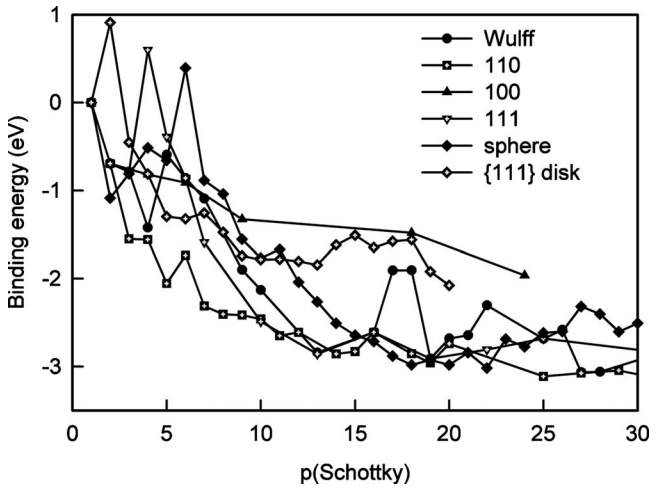

FIG. 6. Binding energies (as defined by Eq. (7)) of different shapes of void as a function of the p number of S defects. The lines have been drawn to guide the eye.

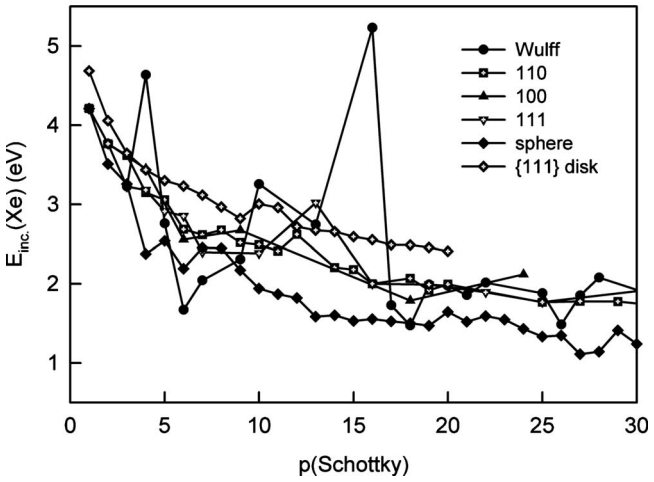

FIG. 7. Xenon incorporation energies (in eV/Xe atom) in different void shapes, as a function of the p number of S defects, which contain p Xe atoms. The lines have been drawn to guide the eye.

the experiments which evidenced that voids are faceted in urania.[54] Nevertheless, for most of the voids the binding energy seems to converge to a value around 3 eV. This means that it is more favorable to create big size voids than to create medium size voids (around 15 S defects).

B. Incorporation of xenon in pre-existing voids

We have substituted each S defect with one xenon atom (with the xenon lying in the uranium site of the S defect) for each type of voids investigated above, as a function of the number p of S defects (up to 30 xenon in 3D voids and up to 20 in disk-shaped voids). The incorporation energies have been calculated by generalization of the Eq. (2), as follow:

$$p\mathrm{Xe} + \mathrm{Void}_{\mathrm{p}}^{\mathrm{S}} \rightarrow \mathrm{Xe(S)}_{\mathrm{p}}$$

with

$$E_{\mathrm{inc}}[\mathrm{Xe(S)}_{\mathrm{p}}] = \{E[\mathrm{Xe(S)}_{\mathrm{p}}] - E(\mathrm{Void}_{\mathrm{p}}^{\mathrm{S}}) - pE(\mathrm{Xe}_{\mathrm{g}})\}/p, \tag{8}$$

where $\mathrm{Xe(S)}_{\mathrm{p}}$ is a void constituted of pS defects containing p atoms of Xe. The xenon incorporation energies in the different types of voids as a function of their size p have been reported on Fig. 7. As observed for voids, the incorporation energies of Xe generally decrease with the size of the voids (i.e., with the number p of xenon atoms). The general behavior of the incorporation energy is comparable for all the types of voids. The incorporation energies slowly converge such that the gain in energy decreases as the size of the voids increases. Three important observations can be made: (i) the behavior of the {100}-shaped voids filled by xenon is close to the other voids, in contradiction with what was observed for empty voids, (ii) the xenon incorporation energies in Wulff-shaped voids are (generally) higher than the other voids, and (iii) the incorporation energies in the spherical voids are (generally) the lowest, particularly after 20 S and unlike what is observed with empty voids. From those three observations, we deduced that the shape of the voids may be different depending on the presence of xenon atoms. The presence of xenon atoms in the voids makes the spherical voids energetically more stable than any other voids investigated here, in agreement with experiments.[12,13] Finally, the number of 20 S—at which the energy convergence for the xenon incorporation is attained—corresponds to a spherical xenon bubble with a radius of 1.3 nm. This radius is comparable to the bubble radius of 1–2 nm found experimentally[12] by transmission electron microscopy in xenon-implanted UO_2 samples.

As done previously for the planar defects, we fitted the xenon incorporation energy in spherical voids and in disk-shaped voids with an analytical expression [Eq. (9)]. We considered neither the Wulff-shaped voids nor the {100}, {110}, and {111} voids as they are less stable than the spherical voids. The total energy of the spherical voids containing xenon atoms as a function of the number p defects can be expressed as follows:

$$E(p) = E_0 + \Omega_{\mathrm{inc}} \times p + \sigma_{\mathrm{inc}} \times p^{2/3} \tag{9}$$

with Ω_{inc} and σ_{inc} being, respectively, the volume and the surface contribution to the energy. The xenon incorporation energy in the pre-existing spherical voids can then be expressed as

$$E_{\mathrm{inc}}(\mathrm{Xe}) = \frac{E(p) - E_0}{p} = \Omega_{\mathrm{inc}} + \frac{\sigma_{\mathrm{inc}}}{\sqrt[3]{p}}. \tag{10}$$

With the surface (δ_{inc}) and line contributions (λ_{inc}), the incorporation energies of the disk-shaped voids read as

$$E_{\mathrm{inc}}(\mathrm{Xe}) = \delta_{\mathrm{inc}} + \frac{\lambda_{\mathrm{inc}}}{\sqrt{p}}. \tag{11}$$

The fittings give Ω_{inc}=0.28 eV/Xe and σ_{inc}=4.55 for the incorporation in spherical voids and δ_{inc}=1.66 eV/Xe and λ_{inc}=3.60 for the incorporation in disk-shaped voids. It means that when the size of the void containing xenon atoms is large enough (i.e., when $p \rightarrow +\infty$), the incorporation energy

tends to the value of 0.28 eV/Xe for spherical voids and 1.66 eV/Xe for disk-shaped voids.

VI. CONCLUSION AND DISCUSSION

First-principles calculations have been carried out to calculate the incorporation energies of xenon atoms in point defects in urania. As previously shown by other authors xenon atoms are more stable in neutral defects (Schottky). Based on these data, empirical potentials have been fitted for the Xe-O and Xe-U interactions. With this set of parameters, static calculations have been carried out to investigate the incorporation of xenon atoms in extended planar interstitials, faceted and spherical voids. It has been found that nanovoids, with or without xenon atoms, are more likely to aggregate into clusters than be homogeneously distributed in the grain. For the extended defects, xenon atoms stabilize more favorably in $\Sigma 5$ grain boundary $[E_{\mathrm{inc}}(\infty)=0.07\ \mathrm{eV/Xe}]$ or spherical shape voids $[E_{\mathrm{inc}}(\infty)=0.28\ \mathrm{eV/Xe}]$. Note that both incorporation energies are positive, xenon atoms still remain insoluble in UO_2 which is in agreement with the experimental observations.

Two interesting insights may be extracted from the results presented herein, considering that the incorporation energies in nanovoids and $\Sigma 5$ grain boundary are similar. First, we may deduce a preference concerning the sites of xenon stabilization: the vacancies created by the irradiations in the bulk of UO_2 are likely filled by xenon and form xenon nanoclusters; whenever those nanoclusters are filled, the xenon atoms stabilize in grain boundaries. This mechanism is in agreement with the macroscopic models. Second, the shape of the xenon clusters is rather spherical than faceted. These results are in agreement with the experimental observations (see, e.g., Refs 8–10) and support the approximation of xenon bubbles as spheres.

Finally, we have to mention that all the results are based on calculations done by static minimizations of the energy in the framework of empirical potentials. Consequently, in those calculations neither the pressure nor the temperature is taken into account. The effect of temperature and pressure will be considered in subsequent papers.

ACKNOWLEDGMENTS

The authors acknowledge funding through the European Commission under the FP7 F-BRIDGE project (Contract No. 211690). Most calculations were carried out at the CCRT computing center of Bruyères-Le-Châtel in France within the framework of the GENCI challenge project (allocation 2009-09c6149).

*Corresponding author; alain.chartier@cea.fr

[1] A. H. Booth, AECL Report No. 496, 1957 (unpublished).
[2] R. J. White and M. O. Tuckern, J. Nucl. Mater. **118**, 1 (1983).
[3] M. S. Veshchunov, J. Nucl. Mater. **277**, 67 (2000).
[4] M. S. Veshchunov and V. E. Shestak, J. Nucl. Mater. **384**, 12 (2009).
[5] M. S. Veshchunov, V. D. Ozrin, V. E. Shestak, V. I. Tarasov, R. Dubourg, and G. Nicaise, Nucl. Eng. Des. **236**, 179 (2006).
[6] L. Noirot, J. Nucl. Sci. Technol. **43**, 1149 (2006).
[7] K. Govers, S. Lemehov, and M. Verwerft, J. Nucl. Mater. **374**, 461 (2008).
[8] K. Nogita and K. Une, J. Nucl. Sci. Technol. **30**, 900 (1993).
[9] K. Nogita and K. Une, J. Nucl. Mater. **226**, 302 (1995).
[10] K. Nogita and K. Une, J. Nucl. Mater. **250**, 244 (1997).
[11] G. Sattonnay, L. Vincent, F. Garrido, and L. Thomé, J. Nucl. Mater. **355**, 131 (2006).
[12] P. Martin, P. Garcia, G. Carlot, C. Sabathier, C. Valot, V. Nassif, O. Proux, and J.-L. Hazemann, Nucl. Instrum. Methods Phys. Res. B **266**, 2887 (2008).
[13] C. Sabathier, L. Vincent, P. Garcia, F. Garrido, G. Carlot, L. Thome, P. Martin, and C. Valot, Nucl. Instrum. Methods Phys. Res. B **266**, 3027 (2008).
[14] P. Garcia, P. Martin, G. Carlot, E. Castelier, M. Ripert, C. Sabathier, C. Valot, F. D'Acapito, J.-L. Hazemann, O. Proux, and V. Nassif, J. Nucl. Mater. **352**, 136 (2006).
[15] C. R. A. Catlow, Proc. R. Soc. London, Ser. A **364**, 473 (1978).
[16] R. A. Jackson and C. R. A. Catlow, J. Nucl. Mater. **127**, 167 (1985).
[17] C. R. A. Catlow and R. W. Grimes, J. Nucl. Mater. **165**, 313 (1989).
[18] R. W. Grimes and C. R. A. Catlow, Philos. Trans. R. Soc. London, Ser. A **335**, 609 (1991).
[19] D. Schwen, M. Huang, P. Bellon, and R. S. Averback, J. Nucl. Mater. **392**, 35 (2009).
[20] D. C. Parfitt and R. W. Grimes, J. Nucl. Mater. **392**, 28 (2009).
[21] H. Y. Geng, Y. Chen, Y. Kaneta, and M. Kinoshita, J. Alloys Compd. **457**, 465 (2008).
[22] J. P. Perdew, K. Burke, and M. Ernzerhof, Phys. Rev. Lett. **77**, 3865 (1996).
[23] P. E. Blöchl, Phys. Rev. B **50**, 17953 (1994).
[24] J. Hafner, J. Comput. Chem. **29**, 2044 (2008).
[25] M. Freyss, N. Vergnet, and T. Petit, J. Nucl. Mater. **352**, 144 (2006).
[26] N. Troullier and J. L. Martins, Phys. Rev. B **43**, 1993 (1991).
[27] S. L. Dudarev, G. A. Botton, S. Y. Savrasov, Z. Szotek, W. M. Temmerman, and A. P. Sutton, Phys. Status Solidi A **166**, 429 (1998).
[28] I. D. Prodan, G. E. Scuseria, and R. L. Martin, Phys. Rev. B **73**, 045104 (2006).
[29] Y. Yun, Ph.D. thesis, University of Kyung Hee, 2006.
[30] M. Iwasawa, Y. Chen, Y. Kaneta, T. Ohnuma, H.-Y. Geng, and M. Kinoshita, Mater. Trans. **47**, 2651 (2006).
[31] F. Gupta, G. Brillant, and A. Pasturel, Philos. Mag. **87**, 2561 (2007).
[32] P. Nerikar, T. Watanabe, J. S. Tulenko, S. R. Phillpot, and S. B. Sinnott, J. Nucl. Mater. **384**, 61 (2009).
[33] B. Dorado, M. Freyss, and G. Martin, Eur. Phys. J. B **69**, 203 (2009).
[34] P. V. Nerikar, X.-Y. Liu, B. P. Uberuaga, C. R. Stanek, S. R. Phillpot, and S. B. Sinnott, J. Phys.: Condens. Matter **21**,

435602 (2009).
[35] J. Yu, R. Devanathan, and W. J. Weber, J. Phys.: Condens. Matter **21**, 435401 (2009).
[36] B. Dorado, B. Amadon, M. Freyss, and M. Bertolus, Phys. Rev. B **79**, 235125 (2009).
[37] Y. Yun, H. Kim, H. Kim, and K. Park, J. Nucl. Mater. **378**, 40 (2008).
[38] D. Morelon, N. D. Ghaleb, J.-M. Delaye, and L. Van Brutzel, Philos. Mag. **83**, 1533 (2003).
[39] J. P. Crocombette, F. Jollet, L. Thien Nga, and T. Petit, Phys. Rev. B **64**, 104107 (2001).
[40] Hj. Matzke, J. Chem. Soc. Faraday Trans. 2 **83**, 1121 (1987).
[41] K. Govers, S. Lemehov, and M. Hou, J. Nucl. Mater. **376**, 66 (2008).
[42] K. T. Tang and J. P. Toennies, J. Chem. Phys. **118**, 4976 (2003).
[43] J. A. Beattie, R. J. Barriault, and J. S. Brierley, J. Chem. Phys. **19**, 1219 (1951).
[44] A. N. Zisman, I. V. Aleksandrov, and S. M. Stishov, Phys. Rev. B **32**, 484 (1985).
[45] J. D. Gale and A. L. Rohl, Mol. Simul. **29**, 291 (2003).
[46] G. Wulff, Z. Kristallogr. Mineral. **34**, 449 (1901).
[47] P. W. Tasker, J. Phys. C **12**, 4977 (1979).
[48] M. Abramowski, R. W. Grimes, and S. Owens, J. Nucl. Mater. **275**, 12 (1999).
[49] L. Van Brutzel and E. Vincent-Aublant, J. Nucl. Mater. **377**, 522 (2008).
[50] S. von Alfthan, P. D. Haynes, K. Kaski, and A. P. Sutton, Phys. Rev. Lett. **96**, 055505 (2006).
[51] Y. Lei, Y. Ito, N. D. Browning, and T. J. Mazanec, J. Am. Ceram. Soc. **85**, 2359 (2002).
[52] R. C. Cammarata and K. Sieradzki, Phys. Rev. Lett. **62**, 2005 (1989).
[53] F. H. Streitz, R. C. Cammarata, and K. Sieradzki, Phys. Rev. B **49**, 10707 (1994).
[54] M. R. Castell, Phys. Rev. B **68**, 235411 (2003).
[55] A. H. H. Tan, M. Abramowski, R. W. Grimes, and S. Owens, Phys. Rev. B **72**, 035457 (2005).
[56] E. Vincent-Aublant, J. M. Delaye, and L. Van Brutzel, J. Nucl. Mater. **392**, 114 (2009).